Epitaxial Growth of Shape-Controlled Bi$_2$Te$_3$−Te Heterogeneous Nanostructures

Wenshou Wang,[†,‡] James Goebl,[†] Le He,[†] Shaul Aloni,[§] Yongxing Hu,[†]
Liang Zhen,[‡] and Yadong Yin*,[†]

*Department of Chemistry, University of California, Riverside, California 92521, United States,
School of Materials Science and Engineering, Harbin Institute of Technology, Harbin, 150001,
People's Republic of China, and The Molecular Foundry, Lawrence Berkeley National
Laboratory, Berkeley, California 94720, United States*

Received September 10, 2010; E-mail: yadong.yin@ucr.edu

Abstract: A one-pot solution process has been devised to synthesize colloidal Bi$_2$Te$_3$−Te heterogeneous nanostructures (HNs) that comprise Bi$_2$Te$_3$ nanoplates and Te nanorods. By controlling the reaction kinetics, the reaction of TeO$_3^{2-}$ and Bi^{3+} in the presence of hydrazine first produces uniform Te nanorods and then grows Bi$_2$Te$_3$ nanoplates on the tips and surfaces of these Te nanorods, forming various shapes including "nails", "barbells", "syringes", and "accordions". The specific topological arrangement realized arises from the peculiar anisotropic reactivity of the first formed Te nanorods, whose tips are subsequently exploited to seed the heterogeneous nucleation of Bi$_2$Te$_3$ as enabled by the similar crystal structure and the small lattice mismatch between Te and Bi$_2$Te$_3$. Three important processes, heterogeneous nucleation of Bi$_2$Te$_3$ on the tips and/or surface of Te nanorods, homogeneous nucleation of Bi$_2$Te$_3$, and the direct reaction of a Bi precursor and Te nanorods to form hollow structures via the Kirkendall Effect, occur under various conditions. The manipulation of these processes provides a robust means for the fine shape control of Bi$_2$Te$_3$−Te HNs. It is envisioned that the tailored synthesis of Bi$_2$Te$_3$−Te HNs may promise unique opportunities for producing thermoelectric materials with greatly enhanced performance.

1. Introduction

Colloidal inorganic nanocrystals have been intensively studied in the past two decades because of their interesting size-/shape-dependent electrical, optical, magnetic, and chemical properties that cannot be achieved by their bulk counterparts.[1−5] Solution phase chemical routes have been successfully developed as a group of general procedures for the preparation of a large variety of nanocrystalline materials with well-controlled sizes and shapes.[6−14] While earlier works mostly focused on single-phase materials, recent efforts have been directed toward the rational synthesis of nanocrystals that are heterogeneous in composition and structure in order to take advantage of the combined properties and functions that are associated with different components of the particles.[15−20] It has also been found that hybrid nanostructures formed by chemically joining two or more inorganic materials can be technologically advantageous in many cases because they exhibit intriguing properties that are distinct from the simple mixture of corresponding single-phase particles.[15−18]

Indeed, the formation of heterogeneous nanostructures represents another powerful means, in addition to the control over composition, size, and shape, for tailoring the properties of nanoscale materials.[21−27] One class of typical heterogeneous nanostructures is synthesized by selective growth of metal or semiconductor dots such as Au, Ag, Pt, Co, PbSe, or ZnSe on the tips of presynthesized nanorods of CdS or CdSe, with the final shape being analogous to either dumbbells or matchsticks.[28−40]

† University of California.
‡ Harbin Institute of Technology.
§ Lawrence Berkeley National Laboratory.
(1) Yin, Y.; Alivisatos, A. P. *Nature* **2005**, *437*, 664.
(2) Park, J.; Joo, J.; Kwon, S. G.; Iang, Y.; Hyeon, T. *Angew. Chem., Int. Ed.* **2007**, *46*, 4630.
(3) Jun, Y.; Choi, J.; Cheon, J. *Angew. Chem., Int. Ed.* **2006**, *45*, 3414.
(4) Tao, A.; Habas, S.; Yang, P. *Small* **2008**, *4*, 310.
(5) Lim, B.; Jiang, M. J.; Tao, J.; Camargo, P.; Zhu, Y. M.; Xia, Y. N. *Adv. Funct. Mater.* **2009**, *19*, 189.
(6) Peng, X.; Manna, L.; Yang, W.; Wickham, J.; Scher, E.; Kadavanich, A.; Alivisatos, A. P. *Nature* **2000**, *404*, 59.
(7) Puntes, V. F.; Krishnan, K. M.; Alivisatos, A. P. *Science* **2001**, *291*, 2115.
(8) Sun, S.; Murray, C.; Weller, D.; Folks, L.; Moser, A. *Science* **2000**, *287*, 1989.
(9) Joo, J.; Na, H. Y.; Yu, T.; Yu, J. H.; Kim, Y. W.; Wu, F.; Zhang, J. Z.; Hyeon, T. *J. Am. Chem. Soc.* **2003**, *125*, 11100.
(10) Panthani, M.; Akhavan, V.; Goodfellow, B.; Schmidtke, J.; Dunn, L.; Dodabalapur, A.; Barbara, P.; Korgel, B. *J. Am. Chem. Soc.* **2008**, *130*, 16770.
(11) Mokari, T.; Zhang, M.; Yang, P. *J. Am. Chem. Soc.* **2007**, *129*, 9864.
(12) Mai, H.; Zhang, Y.; Si, R.; Yan, Z.; Sun, L.; You, L.; Yan, C. *J. Am. Chem. Soc.* **2006**, *128*, 6426.
(13) Lu, A.; Salabas, E.; Schuth, F. *Angew. Chem., Int. Ed* **2007**, *46*, 1222.
(14) Wang, X.; Zhuang, J.; Peng, Q.; Li, Y. *Nature* **2005**, *437*, 121.
(15) Cao, Y.; Banin, U. *J. Am. Chem. Soc.* **2000**, *122*, 9692.
(16) Zeng, H.; Li, J.; Wang, Z.; Liu, J.; Sun, S. *Nano Lett.* **2004**, *4*, 187.
(17) Gu, H.; Zheng, R.; Zhang, X.; Xu, B. *J. Am. Chem. Soc.* **2004**, *126*, 5664.
(18) Gu, H.; Yang, Z.; Gao, J.; Chang, C.; Xu, B. *J. Am. Chem. Soc.* **2005**, *127*, 34.
(19) Gao, X.; Yu, L.; MacCuspie, R.; Matsui, H. *Adv. Mater.* **2005**, *17*, 426.
(20) Rodringuez-Gonzalez, B.; Brrows, A.; Watanabe, M.; Kiely, C.; Marzan, L. *J. Mater. Chem.* **2005**, *15*, 1755.
(21) Mieszawska, A.; Jalilian, R.; Sumanasekera, G.; Zamborini, F. *Small* **2007**, *3*, 722.

The dots at the tips bring new properties to the nanorods, for example, by serving as recognition elements for directed self-assembly, improving contact with electric circuitry,[28,41] and greatly enhancing the electric conductance of the system.[42] As most syntheses are carried out through a two-step seeded growth procedure, the availability of uniform nanostructured precursors such as nanorods has been a limiting factor which prevents the wide exploration of this synthetic strategy. The development of heterogeneous nanostructures is therefore still in its primitive stages, and full control over the synthesis needs to be further understood and demonstrated. For instance, most secondary growth is limited to dots with spherical shapes, while the growth of anisotropic secondary structures has been rarely reported.[38] It has also been challenging to control the location of the secondary growth on the existing nanostructures, although such a possibility has been hinted at in some recent works.[43,44]

The fabrication of advanced thermoelectric materials with high figures of merit (ZT) has received great attention due to their potential applications in cooling and power generation devices.[45−50] Both theoretical simulations and experimental investigations have recently suggested that thermoelectric materials with high ZTs can be obtained from low-dimensional nanostructures due to both the high density of states and increased phonon scattering, or reduced lattice thermal conductivity, in nanosystems.[51−53] Bismuth telluride (Bi_2Te_3) is currently the best thermoelectric material for solid-state cooling devices because it possesses the highest known ZT at room temperature.[54−56] In contrast, tellurium is an important narrow-band-gap semiconductor with a band gap of 0.3 eV and is considered to be an excellent candidate for applications in highly efficient photoconductors as well as thermoelectric and piezo-electric devices.[57−59] The development of heterogeneous nanostructures (HNs) of these two semiconductors would allow manipulation of the boundary scattering of phonons as well as the overall electrical conductivity, thereby providing many new opportunities for enhancing the thermoelectric efficiency of these materials.[60,61] In order to explore the potential benefits of these heterostructures and to systematically study the contribution of various types of boundaries, the first step is to develop a synthetic method that enables the convenient production of uniform Bi_2Te_3−Te HNs with highly controllable sizes and morphologies. This is a great challenge, however, because it has been difficult to synthesize high quality nanostructures even for the individual single-phase Bi_2Te_3 materials.[62−66]

Herein, we report a one-pot solution route for the synthesis of Bi_2Te_3−Te nanoplate−nanorod HNs through the controlled epitaxial growth of Bi_2Te_3 hexagonal nanoplates on the tips of Te nanorods. The key to this process is controlling the rates of the competing reactions for the formation of Te and Bi_2Te_3 so that uniform Te nanorods are produced first and then Bi_2Te_3 nanoplates are grown on the tips of the nanorods. By carefully adjusting the reaction kinetics, the size, number, and location of the Bi_2Te_3 nanoplates can be controlled, thus forming HNs with a range of different shapes including nails, barbells, syringes, and accordions. We have investigated the formation mechanism of these Bi_2Te_3−Te nanoplate−nanorod HNs and found that the anisotropic growth of Bi_2Te_3 nanoplates on the tips of the Te nanorods is made possible by the small lattice mismatch between the (0001) planes of Te and Bi_2Te_3. To the best of our knowledge, this is the first example of anisotropic growth of secondary nanostructures at the tips of nanorods in a solution phase.

(22) Lauhon, L.; Gudiksen, M.; Wang, D.; Lieber, C. *Nature* **2002**, *420*, 57.
(23) Han, W.; Yi, L.; Zhao, N.; Tang, A.; Gao, M.; Tang, Z. *J. Am. Chem. Soc.* **2008**, *130*, 13152.
(24) Teranishi, T.; Inoue, Y.; Nahaya, M.; Oumi, Y.; Sano, T. *J. Am. Chem. Soc.* **2004**, *126*, 9914.
(25) Milliron, D.; Hughes, S.; Cui, Y.; Manna, J.; Wang, L.; Alivisatos, A. *Nature* **2004**, *430*, 190.
(26) Park, S.; Lim, J.; Chung, S.; Mirkin, C. *Science* **2004**, *303*, 348.
(27) Zhan, J.; Bando, Y.; Hu, J.; Liu, Z.; Yin, L.; Golberg, D. *Angew. Chem., Int. Ed.* **2005**, *44*, 2140.
(28) Mokari, T.; Rothenberg, E.; Popov, I.; Costi, R.; Banin, U. *Science* **2004**, *304*, 1787.
(29) Mokari, T.; Sztrum, C.; Salant, A.; Barani, E.; Banin, U. *Nat. Mater.* **2005**, *4*, 855.
(30) Pacholski, C.; Kornowski, A.; Weller, H. *Angew. Chem., Int. Ed.* **2004**, *43*, 4774.
(31) Cozzoli, P.; Pellegrino, T.; Manna, L. *Chem. Soc. Rev.* **2006**, *35*, 1195.
(32) Halpert, J.; Porter, V.; Zimmer, J.; Bawendi, M. *J. Am. Chem. Soc.* **2006**, *128*, 12590.
(33) Kudera, S.; Carbone, L.; Casula, M.; Cingolani, R.; Falqui, A.; Snoeck, E.; Parak, W.; Manna, L. *Nano Lett.* **2005**, *5*, 445.
(34) Carbon, L.; Kudera, S.; Giannini, C.; Ciccarella, G.; Cingolani, R.; Cozzoli, P.; Manna, L. *J. Mater. Chem.* **2006**, *16*, 3952.
(35) Wetz, F.; Soulantica, K.; Faqui, A.; Respaud, M.; Snoeck, E.; Chaudret, B. *Angew. Chem., Int. Ed.* **2007**, *46*, 7079.
(36) Habas, S.; Yang, P.; Mokari, T. *J. Am. Chem. Soc.* **2008**, *130*, 3294.
(37) Deka, S.; Falqui, A.; Bertoni, G.; Sangregorio, C.; Poneti, G.; Morello, G.; Giorgi, M.; Giannini, C.; Cingolani, R.; Manna, L.; Cozzoli, P. *J. Am. Chem. Soc.* **2009**, *131*, 12817.
(38) Maynadie, J.; Salant, A.; Falqui, A.; Respaud, M.; Shaviv, E.; Banin, U.; Soulantica, K.; Chaudret, B. *Angew. Chem., Int. Ed.* **2009**, *48*, 1814.
(39) Kirsanova, M.; Nemchinov, A.; Hewa-Kasakarage, N.; Schmall, N.; Zamkov, M. *Chem. Mater.* **2009**, *21*, 4305.
(40) O'Sullivan, C.; Gunning, R.; Sanyal, A.; Barrett, C.; Geaney, H.; Laffir, F.; Ahmed, S.; Ryan, K. *J. Am. Chem. Soc.* **2009**, *131*, 5218.
(41) Salant, A.; Amtay-Sadovsky, E.; Banin, U. *J. Am. Chem. Soc.* **2006**, *128*, 10006.
(42) Sheldon, M.; Trudeau, P.-E.; Mokari, T.; Wang, L.-W.; Alivisatos, A. *Nano Lett.* **2009**, *9*, 3676.
(43) Robinson, R.; Sadtler, B.; Demchenko, D.; Erdonmez, C.; Wang, L.-W.; Alivisatos, A. *Science* **2007**, *317*, 355.
(44) Demchenko, D.; Robinson, R.; Sadtler, B.; Erdonmez, C.; Alivisatos, A.; Wang, L.-W. *ACS Nano* **2008**, *2*, 627.
(45) DiSalvo, F. *Science* **1999**, *285*, 703.
(46) Sales, B. *Science* **2002**, *295*, 1248.
(47) Wang, J.; Gao, Y.; Kim, J. W.; He, Y.; Song, R.; Ahn, C. W.; Tang, Z. *Phys. Chem. Chem. Phys.* **2010**, *12*, 11900.
(48) Goldsmid, H. *Thermoelectric Refrigeration*; Plenum: New York, 1964.
(49) Mahan, G.; Sofo, J. *Proc. Natl. Acad. Sci. U.S.A.* **1996**, *93*, 7436.
(50) Hicks, L.; Dresselhaus, M. *Phys. Rev. B* **1993**, *47*, 16631.
(51) Venkatasubramanian, R.; Siivola, E.; Colpitts, T.; O'Quinn, B. *Nature* **2001**, *413*, 597.
(52) Harman, T.; Taylor, P.; Walsh, M.; LaForge, B. *Science* **2002**, *297*, 2229.
(53) Harman, T.; Taylor, P.; Spears, D.; Walsh, M. *J. Electron. Mater.* **2000**, *29*, L1.
(54) Hicks, L.; Dresselhaus, M. *Phys. Rev. B* **1993**, *47*, 16631.
(55) Borca-Tasciuc, D.; Chen, G.; Prieto, A.; Martin-Gonzalez, M.; Stacy, A.; Sands, T.; Ryan, M.; Fleurial, J. *Appl. Phys. Lett.* **2004**, *85*, 6001.
(56) Tritt, T.; Subramanian, M. *MRS Bull.* **2006**, *31*, 188.
(57) Mayers, B.; Xia, Y. *J. Mater. Chem.* **2002**, *12*, 1875.
(58) Mohanty, P.; Kang, T.; Kim, B.; Park, J. *J. Phys. Chem. B* **2006**, *110*, 791.
(59) Chaudhyri, S.; Chakrabarti, B.; Pal, A. *Thin Solid Film* **1981**, *82*, 217.
(60) Lu, W.; Ding, Y.; Chen, Y.; Wang, Z.; Fang, J. *J. Am. Chem. Soc.* **2005**, *127*, 10112.
(61) Wang, W.; Lu, X.; Zhang, T.; Zhang, G.; Jiang, W.; Li, X. *J. Am. Chem. Soc.* **2007**, *129*, 6702.
(62) Purkayastha, A.; Kim, S.; Gandhi, D.; Ganesan, P.; Borca-Tasciuc, T.; Ramanath, G. *Adv. Mater.* **2006**, *18*, 2958.
(63) Ge, J.; Li, Y. *J. Mater. Chem.* **2003**, *13*, 911.
(64) Purkayastha, A.; Lupo, F.; Kim, S.; Borca-Tasciuc, T.; Ramanath, G. *Adv. Mater.* **2006**, *18*, 496.
(65) Xiao, F.; Yoo, B.; Lee, K.; Myung, N. *J. Am. Chem. Soc.* **2007**, *129*, 10068.
(66) Deng, Y.; Nan, C.; Wei, G.; Guo, L.; Lin, Y. *Chem. Phys. Lett.* **2003**, *374*, 410.

2. Experiment

Chemicals. Bismuth nitrate pentahydrate was purchased from Alfa Aesar. Ethylene glycol (EG) and iron(III) chloride were purchased from Fisher Scientific. Sodium tellurite, poly(acrylic acid) (PAA, molecular weight 1800), polyvinylpyrrolidone (PVP, molecular weight 55 000), and anhydrous hydrazine (98%) were purchased from Sigma-Aldrich. The anhydrous hydrazine was diluted with distilled water to 2 M for use in reactions. All other chemical reagents were of analytical grade and used as received without further purification.

Synthesis. A $Bi(NO_3)_3$/EG stock solution was prepared by dissolving $Bi(NO_3)_3 \cdot 5H_2O$ (2 mmol) in EG (20 mL) at 100 °C. A Na_2TeO_3/H_2O stock solution was prepared by dissolving Na_2TeO_3 (0.2 mmol) in distilled water (20 mL) at room temperature. An $FeCl_3$/EG stock solution was prepared by dissolving $FeCl_3$ (0.4 mmol) in EG (20 mL) at 100 °C. In a typical procedure, a mixture of $Bi(NO_3)_3$/EG stock solution (1 mL), PAA (3 mmol), PVP (2 mmol), $FeCl_3$/EG stock solution (15 μL), and EG (9 mL) was heated to about 150 °C under a nitrogen atmosphere with vigorous stirring, forming a transparent solution. A stock solution of 150 μL of Na_2TeO_3/H_2O was then injected into the hot mixture. After about 1 min, a certain volume of diluted hydrazine (2 M) was injected quickly and the reaction solution turned black gradually. The resulting mixture was heated at 150 °C for 3 h. Then the solution was cooled to room temperature, and a black precipitate was obtained upon adding 20 mL of acetone and centrifuging at 11 000 rpm for 10 min. The product was washed several times with distilled water and acetone to remove any residual. The final product was dispersed in ethanol or water.
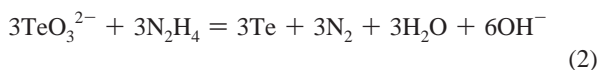
Characterization. Powder X-ray diffraction (XRD) patterns were recorded on a Bruker D8 Advance diffractometer with Cu Kα radiation $\lambda = 1.5406$ Å with a graphite monochromator (40 kV, 40 mA). The morphology of the nanostructures was investigated using a Philips XL30-FEG scanning electron microscope (SEM) and a Tecnai T12 transmission electron microscope (TEM) at an accelerating voltage of 120 kV. The samples for TEM observation were supported on a carbon film covered copper grid. X-ray energy dispersive spectrometer (EDS), high-resolution TEM (HRTEM), and high-angle annular dark field scanning TEM (HAADF-STEM) images were obtained with a JEOL JEM-2100F electron microscope at the Molecular Foundry's Imaging Facility at Lawrence Berkeley National Laboratory. HAADF-STEM images were digitally processed through Gatan Digi-Scan.

3. Results and Discussion

The reaction of TeO_3^{2-} and Bi^{3+} in the presence of a strong reducing agent of hydrazine produces Bi_2Te_3 through the following reaction:

$$6TeO_3^{2-} + 9N_2H_4 + 4Bi^{3+} = 2Bi_2Te_3 + 9N_2 + 18H_2O \quad (1)$$
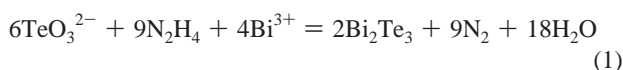
In fact, this reaction can be divided into two sequential steps, including the initial reduction of TeO_3^{2-} to elemental Te and then the further reaction of Te with Bi^{3+} to Bi_2Te_3:

$$3TeO_3^{2-} + 3N_2H_4 = 3Te + 3N_2 + 3H_2O + 6OH^- \quad (2)$$

$$6Te + 3N_2H_4 + 4Bi^{3+} + 12OH^- = 2Bi_2Te_3 + 3N_2 + 12H_2O \quad (3)$$

When the concentration of N_2H_4 is relatively low, its limited reduction power makes Reaction 2 the dominate one which produces mainly Te nanostructures. The anisotropic crystal structure of Te promotes the preferential growth along the ⟨001⟩

direction and leads to the formation of nanorods or nanowires. At a higher concentration of N_2H_4, the reaction may proceed directly to the final product of Bi_2Te_3 without distinctively showing the intermediate step. In order to produce heterogeneous nanostructures, we introduce a small amount of oxidation agent $FeCl_3$ which can temporarily reduce the reduction power of the system so that the reaction at the initial stage produces uniform Te nanorods by following Reaction 2. Subsequent reaction by following Reaction 1 produces Bi_2Te_3 nanoplates which grow epitaxially on existing Te nanorods to form complex heterogeneous structures with nail and barbell shapes. While the epitaxial growth of Bi_2Te_3 nanoplates occurs mainly on the tips of the Te nanorods, it can also occur on the side surfaces of nanorods when the reaction is driven by a high enough concentration of N_2H_4, thus leading to a variety of interesting shapes such as syringes and accordions. If the rod formation reaction and heterogeneous Bi_2Te_3 growth consume most of the Te precursor, the remaining Bi^{3+} ions will react with the existing Te nanorods by following Reaction 3, thus producing hollow nanostructures of Bi_2Te_3 by following the well-known Kirkendall Effect.[67]

3.1. Morphology of Bi_2Te_3−Te HNs. The morphology of Bi_2Te_3−Te HNs is greatly dependent on the amount of hydrazine used in the reaction. Figure 1 shows the representative TEM images of the samples prepared in the presence of 15 μL of the $FeCl_3$/EG stock solution with the addition of different amounts of diluted hydrazine (2 M). All the products are found to be high-quality, uniformly shaped, monodisperse nanocrystalline structures. When only a small amount (130 μL) of N_2H_4 was added, the main product was composed of Te nanorods with lengths of ∼200 nm and diameters of ∼60 nm (Figure 1a and 1b). More careful observation at a higher magnification, as shown in the inset in Figure 1a, reveals very thin nanoplates on either one or both tips of the Te nanorods. As will be revealed in the next section, these nanoplates are Bi_2Te_3 which grows preferentially on tips of the Te nanorods. It is worth noting that the reaction without a bismuth precursor proceeds along Reaction 2, producing long Te nanowires with diameters of ∼50 nm and lengths of tens of micrometers (Figure S1). The formation of nanoplates restricts the axial growth of Te, allows the production of end-capped nanorods with controllable length and morphology. Increasing the amount of hydrazine to 140 μL led to more anisotropic growth of the initially thin nanoplates, producing interesting "barbell"-shaped Bi_2Te_3−Te nanostructures (Figures 1c and 1d). A small fraction of the nanostructures are nail-shaped, probably because of the limited growth on one tip or the breakage of the plate-rod connection during sample preparation. The nanobarbells have an average length of ∼176 nm, and the diameter calculated at the middle of the Te nanorods is ∼40 nm. As bright-field TEM images are a two-dimensional projection of the sample down the optic axis, the Bi_2Te_3 nanoplates appear as rods attached perpendicularly to the Te nanorod. The morphology of Bi_2Te_3 has been confirmed by SEM measurements as hexagonal plates. The insets in Figure 1d are SEM images of the broken barbells, clearly showing the plate structures that are originally attached to the nanorods. It is interesting to note that each nanoplate has a pit at the center which suggests the position where the nanorod was originally attached.

Upon increasing the volume of diluted hydrazine further to 150 μL, the product was composed of mainly nanobarbells and a few nanosyringes, as well as some free nanoplates (Figure 1e

(67) Yin, Y.; Rioux, R.; Erdonmez, C.; Hughes, S.; Somorjai, G.; Alivisatos, A. *Science* **2004**, *304*, 711.
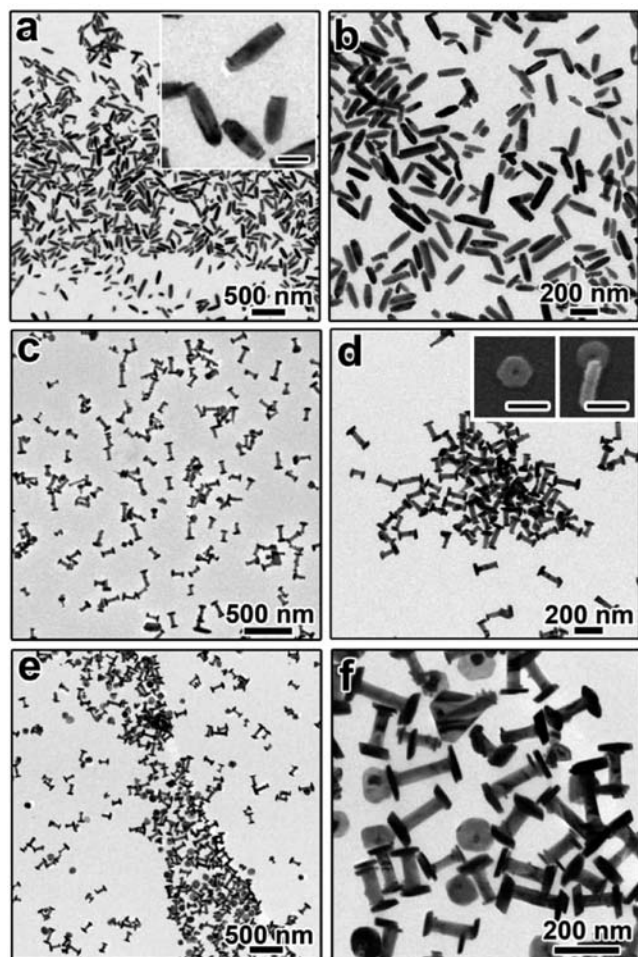
Figure 1. TEM images of the as-prepared samples using different amounts of diluted hydrazine (2 M) in the presence of 15 μL of FeCl₃/EG stock solution: (a, b) 130, (c, d) 140, and (e, f) 150 μL. The insets in (d) are SEM images of a broken barbell structure. The scale bars in the insets of panels (a) and (d) are 100 nm.

and 1f). The nanosyringes display a similar morphology to nanobarbells but contain additional nanoplates perpendicularly grown on the side surfaces of the Te nanorods. The overall dimension of the nanobarbells and nanosyringes remains similar to that of the nanobarbells in Figure 1c, with an average length of 173 nm and a center diameter of 42 nm. As the overall reaction is significantly enhanced with the increased amount of hydrazine in the system, Bi₂Te₃ nanoplates start to nucleate on the side surface of the Te nanorods after both tips have been already occupied. The high concentration of hydrazine may also lead to the homogeneous nucleation of individual Bi₂Te₃ nanoplates. As with many other nanocrystal syntheses, there is a competition between heterogeneous nucleation and homogeneous nucleation for the formation of Bi₂Te₃. At lower concentrations of hydrazine, heterogeneous nucleation is the dominant mechanism which produces Bi₂Te₃─Te HNs. While at higher concentrations of hydrazine, the transient supersaturation of Bi₂Te₃ "monomers" is driven so high that the homogeneous nucleation becomes an additional available pathway which eventually leads to the formation of free nanoplates. It is evident from Figure 1 that varying the amount of added hydrazine provides systematic control of the shape of Bi₂Te₃─Te HNs.

3.2. Structural Characterization. The crystal structures of the various Bi₂Te₃─Te samples were characterized by XRD, and
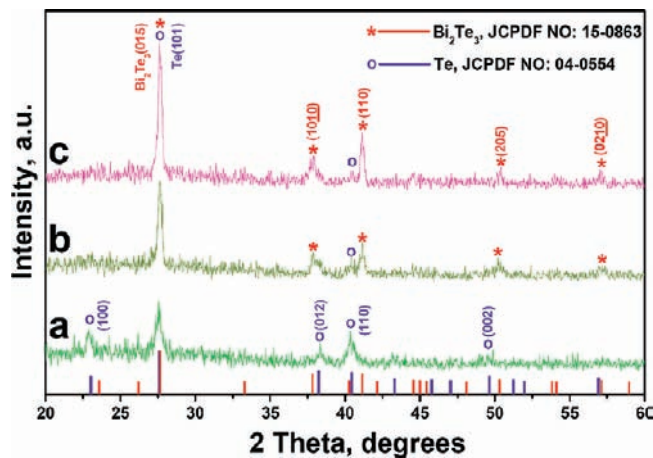

Figure 2. XRD patterns of as-prepared samples using different amounts of diluted hydrazine (2 M) in the presence of 15 μL of FeCl₃/EG stock solution: (a) 130, (b) 140, and (c) 150 μL.

the results are shown in Figure 2. Although their crystal structures are very similar, the standard diffraction peaks of Te (Blue line, JCPDS No. 04-0554, hexagonal phase, with cell constants of $a = 0.4457$ nm and $c = 0.5929$ nm) and Bi₂Te₃ (Red line, JCPDS No. 15-0863, rhombohedral phase, with hexagonal cells of $a = 0.4385$ nm and $c = 3.048$ nm) still display slight differences in peak positions. As shown in Figure 2a, the major diffraction peaks of the sample prepared using 130 μL of 2 M hydrazine can be indexed to hexagonal phase Te. With increasing amounts of hydrazine, the XRD patterns of the as-prepared products (Figure 2b, 2c) suggest the coexistence of Te and Bi₂Te₃. Although those at 27.5° can be assigned to both Te (101) and Bi₂Te₃ (015), the diffraction peaks at 38.2° and 40.5° can be unambiguously indexed to Te (012) and (110), and those at 37.7° and 41.2° can be assigned to Bi₂Te₃ (10$\underline{1}$0) and (110). It is clear that the ratio of diffraction intensity between Bi₂Te₃ (110) and Te (110) increases with the larger volume of added hydrazine, indicating the enhancement in the yield of Bi₂Te₃.

The composition and elemental distribution of the "barbell"-shaped Bi₂Te₃─Te HNs were mapped through EDS by displaying the integrated intensity of bismuth and tellurium signals as a function of the beam position when operating the TEM in scanning mode (STEM). An HAADF-STEM image of an individual Bi₂Te₃─Te nanobarbell is shown in Figure 3a, which reveals a clear contrast between the two nanoplates and the middle nanorod and hints that the "nanobarbell" is composed of two different materials with different morphologies. The respective bismuth and tellurium elemental maps are shown in Figure 3b and 3c, demonstrating well-defined composition variations for the nanobarbells. While both the nanoplates and nanorods display even Te distribution, a strong Bi signal is only obtained from the nanoplates. EDS spectra collected from the selected area of the barbell as indicated by the corresponding circles in Figure 3a are shown in Figure 3d─f. Strong peaks from both Bi and Te with an atomic ratio of ~2:2.9 are found in the plate area (Figure 3d), suggesting the composition of Bi₂Te₃. The atomic ratio of Bi/Te is about 1:24 at the middle of the nanorods, indicating the primary composition of Te. The Cu signals originate from the C-coated Cu TEM grid (C signal is not shown). These elemental mapping and point EDS measurements strongly support the conclusion that the nanoplates are Bi₂Te₃ while the nanorods are Te. Careful inspection of the Bi map shown in Figure 3b reveals that the bismuth
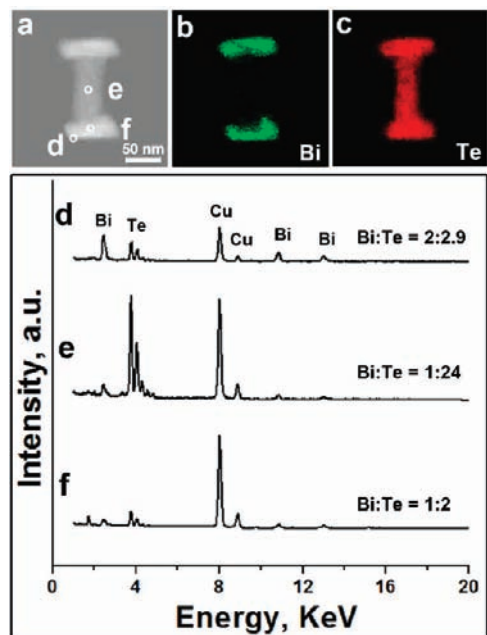
Figure 3. (a) HAADF-STEM image of a typical barbell-shaped Bi_2Te_3−Te nanostructure; (b) Bi and (c) Te elemental maps demonstrating the spatial distribution of Bi and Te elements; (d−f) EDS spectra taken from the regions marked with corresponding white circles shown in (a).

concentration at the interface of the nanoplate and nanorod is low compared to that of the lateral part, with a Bi/Te ratio of ~1:2 (Figure 3f). Various EDS spectra taken from several such areas on other nanobarbells also confirm Bi/Te ratios in the range of 1:3 to 1:2, which are consistent with the composition transition from Te to Bi_2Te_3.

The elemental distribution of the "nanobarbells" can be more clearly appreciated by quantitative atomic percent element mapping, as shown in Figure 4. The color scale ranging from black to white at the bottom in Figure 4b and 4c represents the variation of atomic percentage of the elements. The quantitative mapping of Bi confirms that the rod is Bi deficient while the plates contain an even Bi distribution. However, there is a green-colored notch at the nanorod−nanoplate junction, indicating that this area contains less Bi. Mapping of Te shows that the Te distribution in the middle position of nanorod is ~100%. All these compositional analyses confirm that the barbells are heterogeneous structures each composed of a Te nanorod with two ends capped with Bi_2Te_3 nanoplates.

The crystallographic relationship between the Bi_2Te_3 nanoplates and Te nanorods has been further analyzed by HRTEM measurements. Figure 5a shows an HRTEM image taken at the junction of the Bi_2Te_3 plate and Te rod, while Figure 5b and 5c are images recorded by focusing specifically at the Te and Bi_2Te_3 regions, respectively. The observed lattice spacing of 0.58 nm in Figure 5b corresponds to the (0001) plane of Te, indicating that the single crystalline Te nanorods are of a hexagonal phase with growth along the [0001] direction, which is consistent with previous studies.[68,69] The lattice plane in Figure 5c can be indexed to the (0003) plane of Bi_2Te_3. By comparing the HRTEM images, one can notice that the (0001) Bi_2Te_3 nanoplate lattice planes ($d_{(0001)}$ = 3.40 nm) grow parallel to the direction

of the (0001) lattice planes ($d_{(0001)}$ = 0.59 nm) of the Te nanorod. Prior studies on the epitaxial growth of Bi_2Te_3 on Te have pointed out that the crystallographic orientation between the Te nanorods and Bi_2Te_3 nanoplates can be described as $(0001)_{Te}$// $(0001)_{Bi_2Te_3}$, $[2-1-10]_{Te}$//$[2-1-10]_{Bi_2Te_3}$.[60,70] Therefore, the (0001) planes perpendicular to the crystalline c-axis of Te nanorods serve as starting positions for the epitaxial growth of Bi_2Te_3.

3.3. Formation Mechanism of Bi_2Te_3−Te Nanostructures. The formation of Te nanorods by preferential growth along the c-axis has been well-documented in literature.[68,69] Gao et al. further pointed out recently through *ab initio* calculation that the anisotropic growth of Te nanorods is promoted by the higher adsorption energy of Te atoms on (0001) facets than those on other facets.[70] The preferential growth of Bi_2Te_3 into platelet structures has also been widely reported. Although in this case the anisotropic crystal structure is again believed to dominate the shape of the particles, the sidewise growth, not the axial growth, is considered to be much faster, leading to the formation of thin plates instead of long rods in the Te case.[60,71−73] Therefore, the complex morphology of the Bi_2Te_3−Te HNs reported here is the result of the similar crystal structures but completely different crystal growth behaviors of these two materials.

During the formation of HNs, the positioning of secondary materials on existing nanocrystals has been generally attributed to several factors, including surface defects, differences in the degree of passivation between chemically different facets of the same nanocrystal, lattice mismatch, and the minimization of interfacial energies between the different materials.[28−40] We believe that the close lattice match and minimization of nucleation and interfacial energies for Te and Bi_2Te_3 are the main reasons directing the epitaxial growth of Bi_2Te_3 on Te nanorods. Lattice mismatch is already known to play a significant role in the epitaxial growth of heterogeneous nanostructures via gas-phase deposition, electrodeposition, and solution-phase conformal epitaxial growth.[74,75] Considering the crystal structures of Bi_2Te_3 and Te, the lattice mismatch between Te (0001) and Bi_2Te_3 (0001) is 1.62%, which enables the epitaxial deposition of Bi_2Te_3 on the (0001) facets located on both ends of Te nanorods without causing significant stress. In this case, the preferential growth on the tips is driven by the high surface energy associated with both Te (0001) facets and the sharp curvature at the tip region. Only after the extensive epitaxial growth on the tips, the deposition of Bi_2Te_3 on the side surface of rods becomes possible. However, the lattice mismatch on the side surface is significantly higher, as suggested in a recent study by Fang and Wang on the growth of Bi_2Te_3 plates on long Te rods.[60] As a result, the growth of the epitaxial Bi_2Te_3 layer on the side surfaces follows the Volmer−Weber model, meaning that the deposited materials nucleate as many isolated islands distributed along the rod surface. Subsequent growth of these nuclei leads to the formation of platelets with the surface ((0001) facet) perpendicular to the rod axis. Such a

(68) Tang, Z.; Wang, Y.; Sun, K.; Kotov, N. *Adv. Mater.* **2005**, *17*, 358.
(69) Zhang, B.; Hou, W.; Ye, X.; Fu, S.; Xie, Y. *Adv. Funct. Mater.* **2007**, *17*, 486.
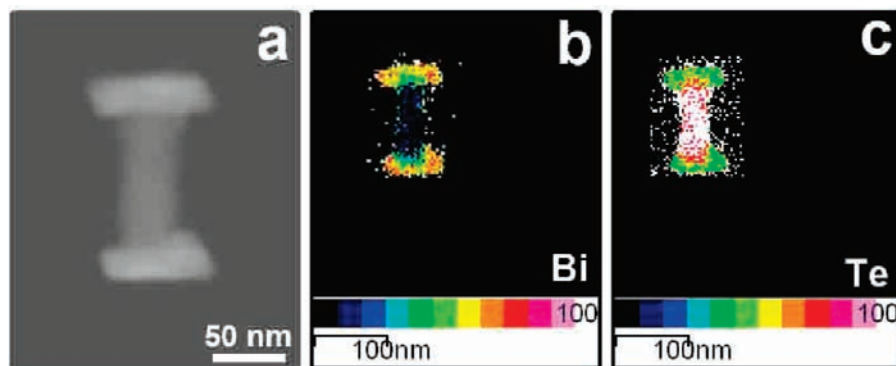
(70) Tian, X.; Du, S.; Gao, H. *Chin. Phys. B* **2008**, *17*, 1674.
(71) Kong, D.; Dang, W.; Cha, J. J.; Li, H.; Meister, S.; Peng, H.; Liu, Z.; Cui, Y. *Nano Lett.* **2010**, *10*, 2245.
(72) Wang, T.; Mehta, R.; Karthik, C. P.; Ganesan, G.; Singh, B.; Jiang, W.; Ravishankar, N.; Borca-Tasciuc, T.; Ramanath, G. *J. Phys. Chem. C* **2010**, *114*, 1796.
(73) Fan, X.; Yang, J.; Xie, Z.; Li, K.; Zhu, W.; Duan, X.; Xiao, C.; Zhang, Q. *J. Phys. D: Appl. Phys.* **2007**, *40*, 5975.
(74) Golan, Y.; Hodes, G.; Rubinstein, I. *J. Phys. Chem.* **1996**, *100*, 2220.
(75) Habas, S.; Lee, H.; Radmilovic, V.; Somorjai, G.; Yang, P. *Nat. Mater.* **2007**, *6*, 692.

Figure 4. (a) HAADF-STEM image of a Bi_2Te_3−Te nanobarbell and corresponding quantitative atomic percent element mapping of elements (b) Bi and (c) Te.
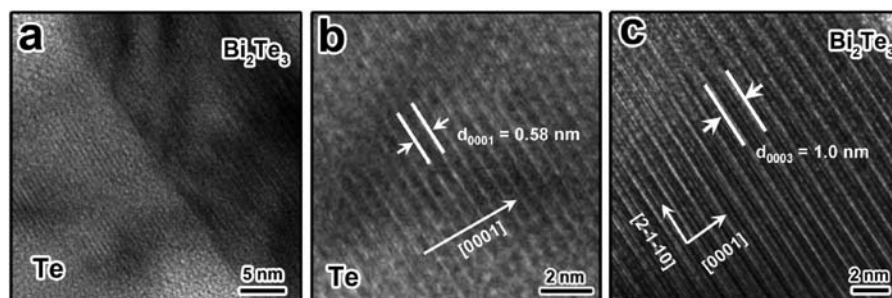

Figure 5. (a) TEM image showing the Bi_2Te_3/Te interface of a nanobarbell structure; (b, c) high-resolution TEM images of (b) Te and (c) Bi_2Te_3.
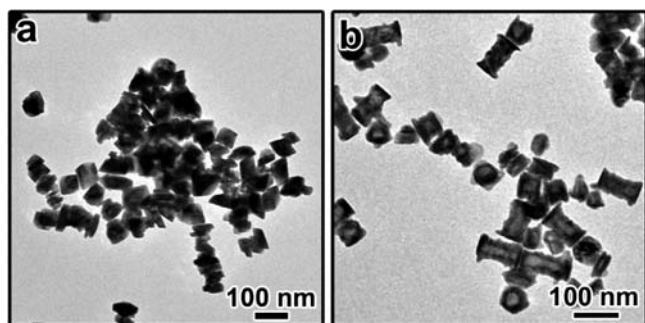

Figure 6. TEM images of samples prepared (a) in the absence of $FeCl_3$ and (b) in the presence of $Fe(NO_3)_3$.

growth model has also been confirmed theoretically through *ab initio* calculation.[70]

Apparently, the size and position of the nanoplates are determined by the concentration of the Bi_2Te_3 "monomers" produced during the reaction. As shown in the following sections, we are able to precisely control the morphology of the HNs by fine-tuning the reaction conditions, including the concentrations of the precursors, the "catalyst" $FeCl_3$, and temperature.

3.4. Role of $FeCl_3$. It was found that the introduction of a trace amount of $FeCl_3$ into the reaction system was indispensable for the formation of well-defined Bi_2Te_3−Te nanobarbells. When the synthesis was performed without using $FeCl_3$, the products were composed of mainly irregular shaped nanoparticles, with few barbell-shaped nanostructures (Figure 6a). Replacing $FeCl_3$ with $NiCl_2$ in a similar quantity results in particles containing only a small amount of barbells, similar to those prepared in the absence of $FeCl_3$. When $Fe(NO_3)_3$ was used instead, the products again contained mainly nanobarbells although the exact size and morphology are different from the case of $FeCl_3$ (Figure

6b). Note that most nanobarbells contain voids, as evidenced by the lower contrast at their center in the TEM images. Since this sample was prepared with a high initial N_2H_4 concentration, Te was consumed quickly and Bi_2Te_3 formed on the surface of Te rods by following Reaction 3. As a result, voids were produced through the nanoscale "Kirkendall Effect", which will be discussed in more detail in the next section. These observations suggest that the presence of Fe^{3+} cations is critical to the formation of Bi_2Te_3−Te "nanobarbell" heterogeneous structures. We believe the presence of Fe^{3+} may temporarily suppress the reducing power of N_2H_4, in a manner similar to that in the synthesis of platinum nanowires and palladium nanostructures reported by Xia and co-workers.[76,77] When a trace amount of Fe^{3+} is introduced, the reduction proceeds mainly by following Reaction 2, producing Te nanorods. When the reducing power of N_2H_4 resumes after the consumption of Fe^{3+}, Bi_2Te_3 becomes the main reaction product which nucleates as plates on the existing Te nanorods, resulting in the final Bi_2Te_3−Te nanobarbells.

3.5. Shape and Size Control of Bi_2Te_3−Te HNs. As the concentrations of both $FeCl_3$ and N_2H_4 affect the reduction rate, it becomes effective to fine-tune the dimension of the nanobarbell structures by adjusting these parameters. A slight decrease in the concentration of $FeCl_3$ from the standard condition enhances the reaction rates and increases the length of Te nanorods. As shown in Figure 7, the samples prepared with 10 μL of $FeCl_3$/EG stock solution were composed of much longer rods compared to the corresponding cases shown in Figure 1 where 15 μL of $FeCl_3$/EG solution were used. As indicated above, the growth of Te is terminated by the epitaxial growth

(76) Cheng, J.; Herricks, T.; Geissler, M.; Xia, Y. *J. Am. Chem. Soc.* **2004**, *126*, 10854.
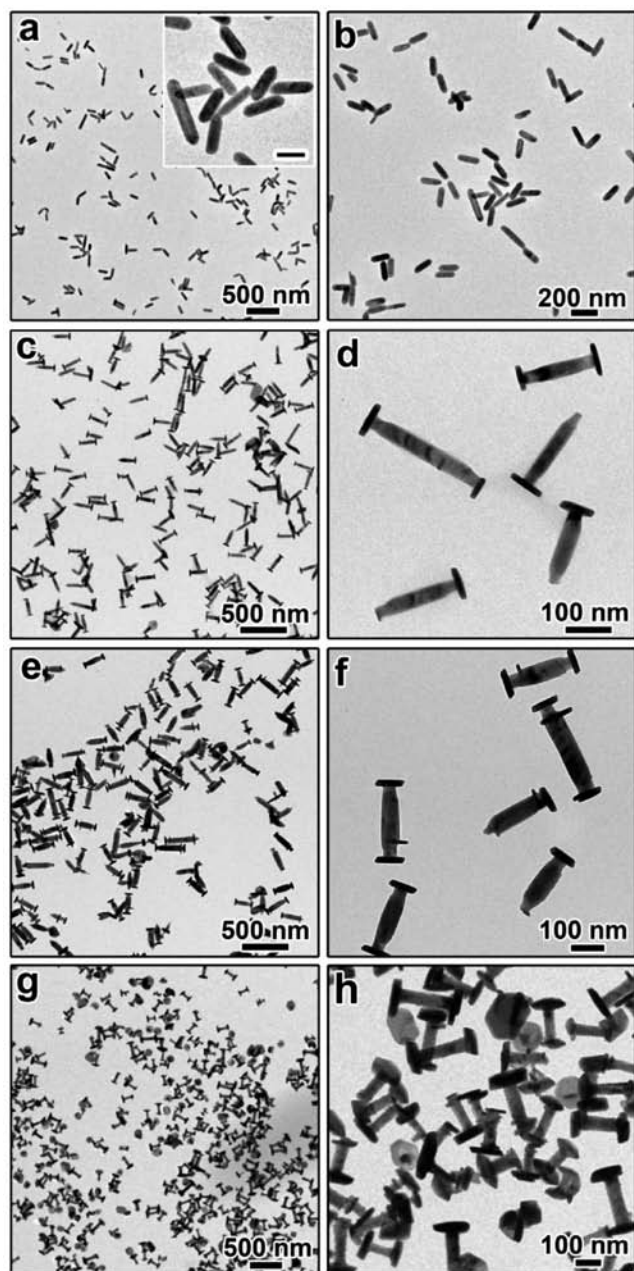(77) Xiong, Y.; McLellan, J.; Chen, J.; Yin, Y.; Li, Z.; Xia, Y. *J. Am. Chem. Soc.* **2005**, *127*, 17118.

Figure 7. TEM images of the as-prepared products using different amounts of diluted hydrazine (2 M) in the presence of 10 μL of FeCl$_3$/EG stock solution: (a, b) 100, (c, d) 130, (e, f) 140, and (g, h) 150 μL. Scale bar of inset is 100 nm.

of Bi$_2$Te$_3$ on both tips. The concentration of N$_2$H$_4$ is therefore another important factor that controls the length of the HNs. When the concentration of FeCl$_3$ is fixed, a higher concentration of N$_2$H$_4$ enhances the rate of heterogeneous nucleation of Bi$_2$Te$_3$, terminates the growth of Te nanorods at an earlier stage, and results in HNs with a smaller overall length. This trend can be observed clearly by comparing the samples shown in Figure 7, where the concentration of N$_2$H$_4$ was systematically varied during the synthesis.

A further increase in the concentration of N$_2$H$_4$ significantly enhances the formation of Te nanorods which quickly exhausts the Te precursor in the system so that the formation of Bi$_2$Te$_3$ follows different pathways. Figure 8 shows the products prepared by adding 170 and 300 μL of 2 M hydrazine. The length of the nanorods continues to decrease with more N$_2$H$_4$,
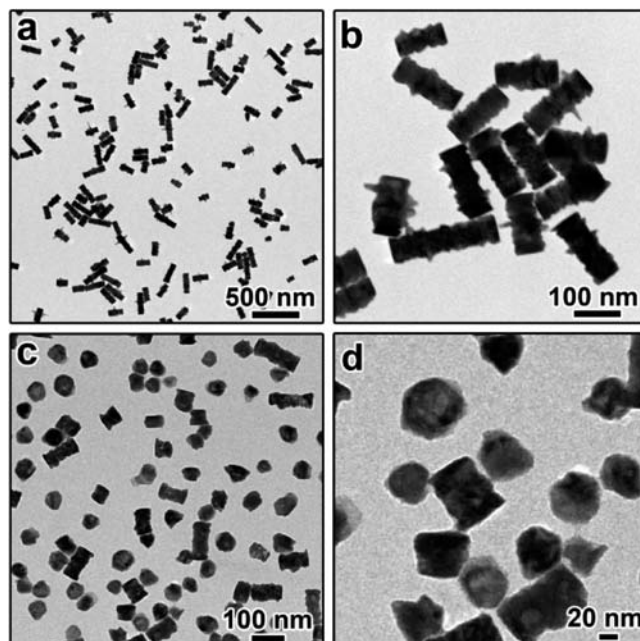

Figure 8. TEM images of as-prepared products in the presence of 10 μL of FeCl$_3$/EG stock solution with (a, b) 170 and (c, d) 300 μL of diluted hydrazine added (2 M).

consistent with prior observation. However, although Bi$_2$Te$_3$ can still cap the tips of Te rods to limit the overall length of the resulting structures, as suggested by the flat ends of the nanorods, its substantial growth into discernible plates cannot be observed. In this case the Te formation through Reaction 2 is so much faster that it consumes most of the TeO$_3^{2-}$ precursor and only allows limited growth of Bi$_2$Te$_3$ through Reaction 1. As a result, the remaining Bi^{3+} can only react with preformed Te nanorods to form Bi$_2$Te$_3$ through Reaction 3. This reaction proceeds by outward diffusion of Te atoms and produces voids inside the Te nanorods through the well-documented nanoscale "Kirkendall Effect".[67] Basically, during this solid−liquid reaction, the inward diffusion of Bi^{3+} is hindered so that Te atoms diffuse out to the interface to form Bi$_2$Te$_3$, thus creating vacancies inside the nanorods. As the reaction proceeds, more vacancies form and eventually condense into large voids, which can be clearly observed in the enlarged TEM images shown in Figure 8b and 8d. A related case can be found in recent literature where the reaction between a Bi precursor and Te nanowires produces Bi$_2$Te$_3$ nanotubes.[78] The interfacial reaction also transforms the originally smooth Te surface into pleated structures, producing "accordion"-shaped Bi$_2$Te$_3$−Te nanostructures.

XRD measurements confirm again that the overall reaction is driven toward pure Bi$_2$Te$_3$ in the presence of an increasing concentration of N$_2$H$_4$, as shown in Figure 9. The main products gradually change from elemental Te at low concentrations of N$_2$H$_4$ to Bi$_2$Te$_3$ at high concentrations of N$_2$H$_4$, as clearly evidenced by the gradual disappearance of Te (012) and (110) peaks at 38.2° and 40.5° and the appearance and strengthening of Bi$_2$Te$_3$ (10$\underline{1}$0) and (110) peaks at 37.7° and 41.2°. Importantly, no distinctive Te diffraction peak can be observed in Figure 9f, suggesting the complete conversion from Te to Bi$_2$Te$_3$ during the hollowing process.

In addition to FeCl$_3$ and N$_2$H$_4$, adjusting the concentration of Bi(NO$_3$)$_3$ also allows us to further fine-tune the morphology

(78) Zhang, G.; Yu, Q.; Yao, Z.; Li, X. *Chem. Commun.* **2009**, 2317.

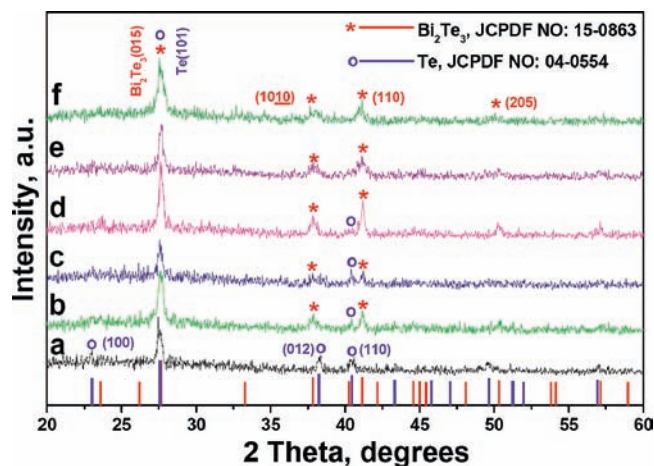**Figure 9.** XRD patterns of as-prepared samples using different amounts of diluted hydrazine (2 M) in the presence of 10 μL of FeCl$_3$/EG stock solution: (a) 100, (b) 130, (c) 140, (d) 150, (e) 170, and (f) 300 μL. The blue and red column lines at the bottom are the standard JCPDS data for Te and Bi$_2$Te$_3$, respectively.
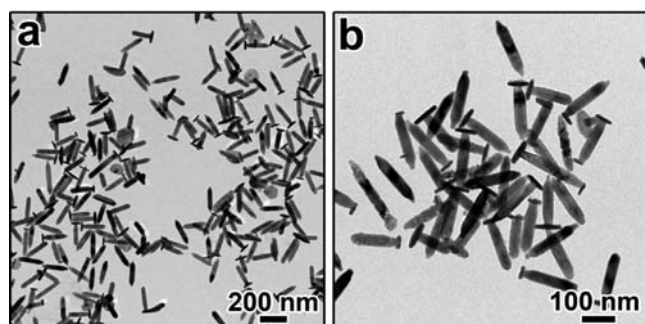

Figure 10. TEM images of "nail"-shaped Bi$_2$Te$_3$—Te nanostructures prepared using 0.08 mmol of Bi(NO$_3$)$_3$ and 130 μL of diluted hydrazine (2 M).

of the HNs. For example, as shown in Figure 10, when the amount of Bi(NO$_3$)$_3$ is slightly reduced to 0.08 mmol from 0.1 mmol in the case of Figure 7c, it is possible to greatly increase the yield of nail-shaped structures. By decreasing the concentration of the Bi, we effectively lower the local concentration of the "monomers" so that the growth of Bi$_2$Te$_3$ is limited to only one end of the Te nanorods, resulting in the formation of nanonails.

3.6. Temperature Effects. As with many chemical syntheses, the reaction temperature also has a significant impact on the morphology of Bi$_2$Te$_3$—Te HNs. Decreasing the reaction temperature from 150 to 130 and 140 °C resulted in the formation of Te nanorods with different lengths, as shown in Figure 11a and 11b, respectively. The Te nanorods prepared at 130 °C have an average diameter of ~30 nm and lengths of 200—500 nm, while those at 140 °C have an average diameter of ~40 nm and lengths of ~200 nm. Although no Bi$_2$Te$_3$ nanoplates can be clearly identified for samples prepared at lower temperatures, the fact that the Te nanorods are shorter at 140 °C than 130 °C may suggest that a small amount of Bi$_2$Te$_3$ has already been produced at 140 °C which capped the tips of the Te nanorods. Significant growth of Bi$_2$Te$_3$ into nanoplates requires higher temperatures to overcome the thermodynamic barrier for the production of Bi$_2$Te$_3$ through Reaction 1. Indeed, upon increasing the reaction temperature to 150 °C, Bi$_2$Te$_3$ is found to nucleate on the Te nanorod tips and grow to nanoplates, forming nail/barbell structures (Figure 11c). The competition between
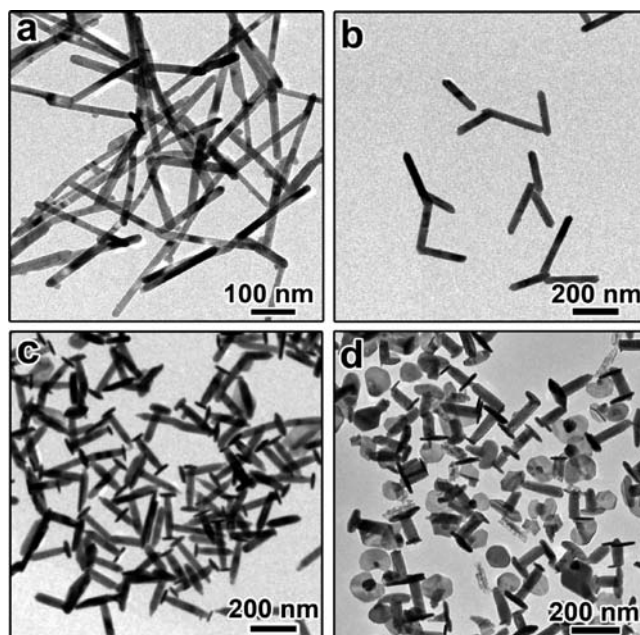

Figure 11. TEM images of the samples prepared using 130 μL of diluted hydrazine (2 M) at different reaction temperatures: (a) 130, (b) 140, (c) 150, and (d) 160 °C.

heterogeneous and homogeneous nucleation of Bi$_2$Te$_3$ becomes apparent upon further increase of the reaction temperature to 160 °C, where heterogeneous nucleation of Bi$_2$Te$_3$ on the tips of Te nanorods and homogeneous nucleation of Bi$_2$Te$_3$ led to a final product containing both nanobarbells and nanoplates, as shown in Figure 11d. The observed shape evolution controlled by reaction temperature is similar to that using different amounts of hydrazine, which also changes the reaction kinetics. It is worth noting that a further increase of the reaction temperature to 170 °C only produces irregular nanoparticles. The reaction rate can also be estimated from the color change of the solution. The initial clear solution gradually became gray-black at low reaction temperature (130—140 °C) and brown-black within several minutes at 150 °C. At 160 °C, the clear solution turned brown-black within a few seconds, suggesting much faster reactions. Therefore, reaction temperature can significantly change the reaction kinetics for the growth process of Te and Bi$_2$Te$_3$. XRD measurements (Figure S2) confirmed that low reaction temperatures (130—140 °C) mainly resulted in Te, while high reaction temperatures (150—160 °C) led to the formation of Bi$_2$Te$_3$—Te heterostructures.

3.7. Functions of PAA and PVP. The synthesis of Bi$_2$Te$_3$—Te HNs involves two polymeric surfactants, PAA and PVP. PAA is used to prevent the hydrolysis of Bi(NO$_3$)$_3$ by the following reaction: Bi^{3+} + 3OH$^-$ = Bi(OH)$_3$. In the absence of PAA, the white precipitate Bi(OH)$_3$ appeared when the reaction temperature was raised to 150 °C before the injection of hydrazine. Adding hydrazine into the white cloudy solution produced a white/black precipitate at the bottom of the flask, which was found to be neither Te nor Bi$_2$Te$_3$ by XRD measurements (Figure S3). In order to prevent the formation of the white precipitate Bi(OH)$_3$ during heating, an acid surfactant, PAA, was added to the reaction system. In this case, the reaction solution remained clear during the heating process, even at high temperatures (180 °C). As an acid, PAA can enhance Reaction 2 and promote the growth of Te into long nanorods. PVP was therefore added to the reaction to control the Te growth and prevent particle aggregation. In a control experiment without

using PVP, a black precipitate was deposited at the bottom of the flask. The products were composed of severely aggregated long nanorods with lengths of ~500 nm and diameters of ~30 nm. Closer examination of the TEM images revealed that some long nanorods are capped with nanoplates (Figure S4). The use of PAA together with PVP therefore allows for the controllable synthesis of Bi_2Te_3−Te HNs with controllable size, tunable morphologies, and high dispersibility in solvents.

4. Conclusions

In summary, we have demonstrated a simple one-pot solution method to synthesize Bi_2Te_3−Te HNs that comprise Bi_2Te_3 nanoplates on the tips of Te nanorods. By carefully controlling the reaction kinetics, Bi_2Te_3−Te heterostructures with "nail", "barbell", "syringe", and "accordion" shapes can be successfully prepared. The specific topological regime achieved has been found to originate from the initial formation of Te nanorods by temporarily suppressing the reduction power of hydrazine using a small amount of the oxidation agent $FeCl_3$. The subsequent nucleation and growth of Bi_2Te_3 nanoplates on the tips and sides of Te nanorods is mainly due to the similar crystal structure and the small lattice mismatch between Te and Bi_2Te_3. The morphology and composition of the HNs can be controlled by changing the reaction kinetics such as temperature and the concentrations of reactants especially hydrazine. The signifi-cance of our work lies not only in providing a robust synthesis for Bi_2Te_3−Te heterostructures with well-controlled morphol-ogies but also in suggesting that an increased level of synthetic sophistication and topological selectivity in heterostructures can be reached by carefully controlling reaction kinetics. It is believed that the as-prepared Bi_2Te_3−Te heterostructures with tailored morphology and composition may serve as new types of materials for improving the thermoelectric performance.

Supporting Information Available: TEM images of samples prepared without $Bi(NO_3)_3$, or surfactants, XRD measurements showing the effects of temperature and surfactants. This material is available free of charge via the Internet at http://pubs.acs.org.

JA108186W